Article │ Received 2 December 2024; Accepted 30 January 2025; Published 20 February 2025
https://doi.org/10.55092/am20250005

Microstructure and mechanical properties of super-invar alloy fabricated by wire-arc additive manufacturing

Shuijun Ye[1], Lindong Xu[2], Yueling Guo[1,*], Xinglong Di[1], Qifei Han[1], Yuanxuan Zheng[1] and Xingchen Li[1]

[1] School of Mechanical Engineering, Beijing Institute of Technology, Beijing, China
[2] School of Mechanical Engineering, Beijing Institute of Aerospace Systems Engineering, Beijing, China

* Correspondence author; E-mail: y.guo@bit.edu.cn.

Highlights:

- Super-invar Fe64-Ni32-Co4 (wt %) alloy is manufactured by additive manufacturing.
- The columnar cellular microstructure is associated with the G/R value for WAAM.
- The mechanical property anisotropy is found for the super-invar alloy via WAAM.
- Low thermal expansion coefficient of 0.265 × 10^{-6} K^{-1} from 20 ℃ to 100 ℃ is achieved.

Abstract: Here, wire-arc additive manufacturing (WAAM) is employed to manufacture a super-invar alloy thin-wall rectangular component. The microstructure is characterized by cellular sub-grains with different morphologies inside the epitaxially grown columnar crystals. Based on the finite element simulation results, the value of the G (the temperature gradient)/R (the solidification rate) during the deposition process is calculated as 1.59 × 10^{8} K·s·m^{-2}, which is associated with the columnar cellular microstructure. The transfer mode of the droplet during the WAAM is liquid bridge transition. The mechanical properties of specimens are anisotropic, and the longitudinal samples are better than transverse samples; the UTS is 398.8 MPa, the YS is 291.4 MPa, and the elongation is 40.8%. The coefficient of thermal expansion (CTE) is measured to be 0.265 × 10^{-6} K^{-1} in the range of 20 ℃ to 100 ℃. The findings provide a reference for the fast fabrication of super-invar alloy components through WAAM, which promotes the applications of super-invar alloy in aerospace.

Keywords: additive manufacturing; wire-arc additive manufacturing; super-invar alloy; microstructure; mechanical properties

1. Introduction

Invar and super-invar alloys, distinguished by their extremely low coefficient of thermal expansion (CTE) below the Curie point (230 °C) [1], have promising applications in fields requiring high dimensional stability, such as electrical communication, aerospace, precision measuring devices, and railway

transport [2–5]. However, the machining of invar and super-invar alloy components is challenging due to their low heat conductivity, high ductility, and noticeable work hardening. Moreover, the aggravated tool wear results in low manufacturing efficiency and high production costs [6]. Such issues are recently addressed by the rapid development of additive manufacturing (AM) technology [3]. It is suitable for producing parts with complex structures and offers a high degree of design freedom and improved manufacturing efficiency [7]. Among the AM family [8], selective laser melting (SLM) and wire-arc additive manufacturing (WAAM) are the popular AM techniques for invar alloys. Huang *et al.* [9] pointed out that the mechanical properties and microstructure of invar alloy via SLM exhibited anisotropy, but the CTE is isotropic, which is insensitive to the microstructure and related to the magnetic properties. Using SLM technique, Wei *et al.* [10] explored the influence of process parameters on the performance of the invar alloy, and finally they recommended a longer laser residence time and shorter laser scanning spacing.

As a directed energy deposition (DED) technique, WAAM combines an electric arc with metal wires [11]. Three types of WAAM processes are distinguished based on the type of welding source [12]: WAAM based on Gas Metal Arc Welding (GMAW), WAAM technology based on Plasma Arc Welding (PAW) and WAAM technology based on Gas Tungsten Arc Welding (GTAW). Compared to SLM (popularly referred to as laser powder bed fusion or LPBF [13]) and laser-directed energy deposition (LDED) [14,15], WAAM features higher deposition rates, inexpensive equipment costs [16], and a better material utilization ratio [17]. Especially, WAAM is favorable for achieving sustainability because of its high deposition efficiency [18].

Jiao *et al.* [19] built thin-walled single-layer invar alloy deposition using the cold metal transfer (CMT) technique, and they found that the reinforced phase NbC could improve the mechanical properties and reduce the CTE. Based on WAAM, Veiga *et al.* [20] proposed that the lower heat input process yields finer grains and higher strengths of the invar alloy. Compared to GMAW, GTAW process is easier to control, which could improve the forming quality of the fabricated parts [21]. At the same time, it is possible to apply the hot-wire technique, which could heat the wire before it enters the molten pool [22], thus providing extra heat to melt the wire [23], reducing the heat input of GTAW and enhancing mechanical properties [24,25].

Compared to invar alloy, super-invar alloy has an exceptionally low CTE, which makes it a better promising for aerospace applications. However, very limited research had been conducted on the additive manufacturing of super-invar alloy. In this study, considering the high melting point of super-invar alloy, we manufactured a thin-wall rectangular sample by the hot-wire technique based on WAAM. We established a numerical simulation model and obtained the temperature gradient and the solidification rate. In addition, we analyzed the transfer of liquid droplets during the manufacturing process and studied the microstructure, mechanical properties, and CTE of the parts after solution and aging treatment.

2. Material and methods

2.1. WAAM processing and subsequent heat treatment

Super-invar alloy wires (Fe64-Ni32-Co4, wt %), with a diameter of 1.6 mm, were used to fabricate alloy specimens by WAAM. The chemical compositions of components were measured by inductively coupled plasma-atomic emission spectrometry (ICP-AES), and the composition results are shown in

Table 1. The substrate material used in the deposition process was 316 stainless steel, and the dimension was 150 (length) × 150 (width) × 10 (thickness) mm.

Table 1. Chemical composition of super-invar alloy components fabricated by WAAM (wt %).

Element	Fe	Ni	Co	Nb	Mn	C	Si	P	S
Content (%)	Bal.	32.62	4.37	0.24	0.12	0.05	0.028	0.02	0.02

The GTAW-type WAAM equipment in this work was developed by Beijing Institute of Technology (BIT). It mainly consisted of a three-axis computer numerical control (CNC) machine tool, a gas tungsten arc welding, a wire feeding mechanism, a workbench, a TIG power source, and a control system. The deposition equipment was shown in Figure 1(a–b). In addition, a resistance power source was integrated into the WAAM system to preheat the wire in advance. It had a connected circuitry when the wire contacted the molten pool or substrate [26]. This produced high resistance heat on the wire due to the high resistivity of the super-invar alloy. During the deposition process, the welding torch and the wire feeding mechanism worked together to manufacture a thin-wall rectangular component with a continuous scanning path on the 316 stainless steel substrate. The experimental parameters of the deposition process were shown in Table 2. In order to guarantee the stability of the process, we observed the molten metal transfer process using a high-speed camera MER2-041-302GC during WAAM processing. After that, the solution treatment was carried out in a YM-60/13 high-temperature chamber furnace for 1 hour at 840 ℃ with water cooling. After that, aging treatment was performed in the TM1210 heat treatment furnace for 1 hour at 315 ℃, followed by air cooling.

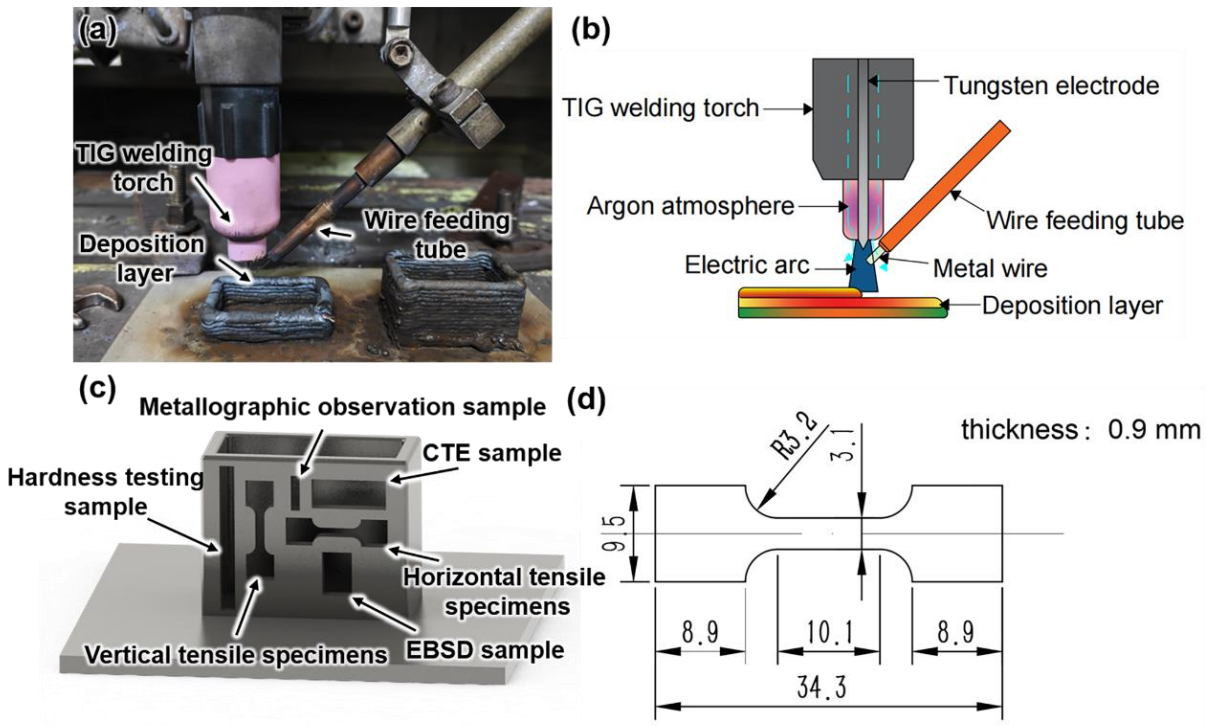

Figure 1. (a) The experimental WAAM setup; **(b)** Sketch of the WAAM deposition process; **(c)** The sampling position for characterization and tensile tests; **(d)** Size of the tensile specimens.

Table 2. Experimental parameters for the WAAM processing of super-invar alloy.

Experimental parameters	Value
Pulse current frequency (Hz)	2
Peak current (A)	234
Peak current time ratio (%)	25
Base to peak current ratio (%)	27
Hot-wire current (A)	150
Feeding speed (cm/min)	170
Travel speed (mm/min)	220
Shield gas flow rate (L/min)	23

2.2. Microstructure characterization, mechanical and physical properties testing

The sampling position for microstructure characterization and mechanical properties testing was shown in Figure 1(c). In order to observe the microstructure of the samples, grinding was carried out on a UNIPOL-820 grinding machine with abrasive papers of 600#, 1200#, 2000#, and 5000#. Next, a polishing machine was used to polish the samples using diamond polishing paste with sizes of 2.5 μm, 1.0 μm, and 0.5 μm, followed by ultrasonic cleaning. The specimens were corroded with chemical etchant (50 ml HCL + 50 ml H_2O + 10 g $CuSO_4$) for about 20 s, and a LW600LJT metallographic microscope was used to examine the microstructure of the specimens. Electro-polishing was carried out on the surface of specimens, which were prepared for the electron backscatter diffraction (EBSD) analysis. In order to gather information on grain structure and orientation, EBSD scanning was carried out using the Nordlys-Max3 detector at a voltage of 20 KV with a scanning step size of 3.5 μm. TSL OIM Analysis 6.0 software was utilized for data analysis.

Hardness was tested by a digital micro-hardness tester (HVST-1000Z) with a load of 200 g and 15 s dwell time. Mechanical properties were characterized using an Instron5966 electronic universal material testing machine at room temperature with a constant loading speed of 0.1 mm/s. The sampling position of the samples for tensile examination was illustrated in Figure 1(c), including both vertical and horizontal directions, and the size of specimens was shown in Figure 1(d). The scanning electron microscope (SEM) was used to analyze the fracture surface and side-view microstructure of fractured tensile specimens. Utilizing a NETZSCH DIL 402SE thermal expansion dilatometer, the cylindrical samples with a 6 mm diameter and 25 mm length were prepared for CTE measurements. The temperature was increased at a rate of 5.0 K/min, ranging from 20 ℃ to 100 ℃.

2.3. Numerical simulation

Using Workbench R2 software, a simplified finite element model for super-invar alloy was developed in order to analyze the evolution of the temperature field. For convenience in the thermal calculation, the following simplifying assumptions were adopted:

(1) Every deposited layer's surface is regarded as flat for modeling purposes.
(2) The heat source type employed in simulation is double-ellipsoidal model [27]. During the deposition process, its effective power and dimensions remain constant.
(3) To simplify the simulation process, in the molten pool, the chemical reactions between elements and stirring effect are disregarded.

The numerical simulation model was mainly composed of ten deposition layers and substrate. In order to improve the efficiency of the finite element model calculation, the mesh's dimensions of the substrate and deposition layers were different; that is, the deposition layers had a more intensive mesh division than the substrate, as shown in Figure 2. The necessary material properties for finite element heat analysis, such as specific heat, heat conductivity, density with temperature, solid phase temperature, and liquid phase temperature, were calculated using JMatPro software, as shown in Figure 2(b–d). Table 3 displayed some parameters in the temperature simulation. The K23E35 infrared thermal imager was used to verify the temperature obtained from thermal simulation.

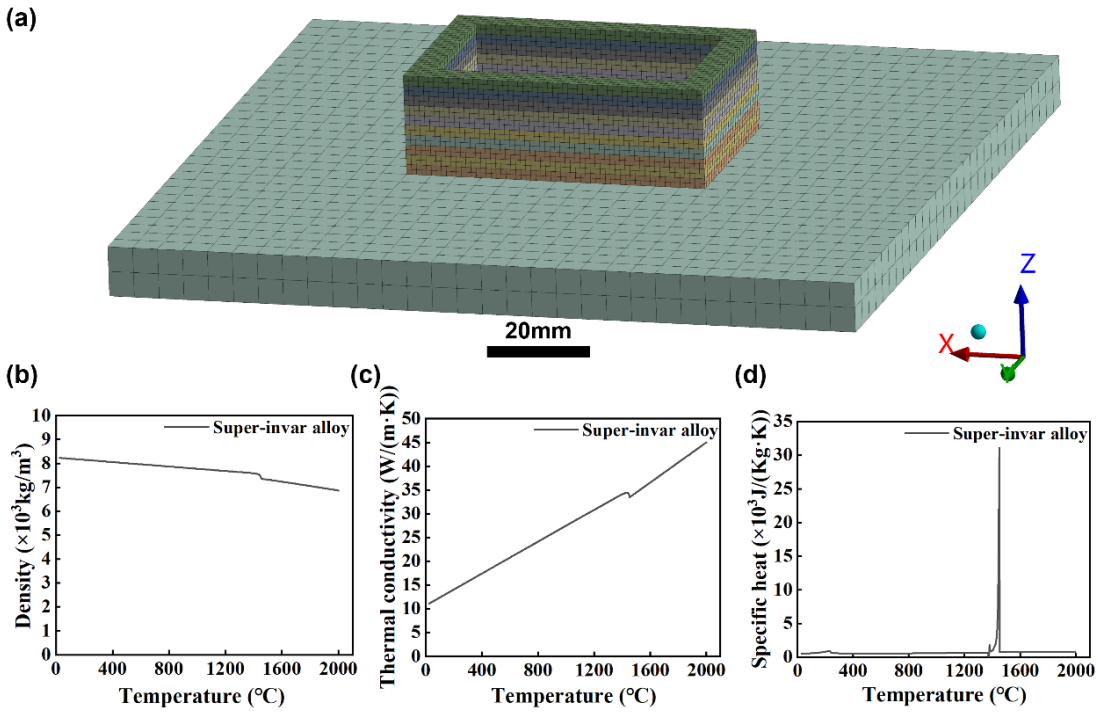

Figure 2. (a) Mesh division of substrate and deposition; **(b)** Curve of material density varying with temperature; **(c)** Curve of material thermal conductivity varying with temperature; **(d)** Curve of material specific heat varying with temperature.

Table 3. Parameters using for numerical simulation.

Parameters	Value
Convective heat transfer coefficient	5.76 $W \cdot m^{-2} \cdot K^{-1}$
Thermal conductivity of the substrate	13.31 $W \cdot m^{-1} \cdot K^{-1}$
Ambient temperature	293.15 K
Initial temperature	293.15 K
The dimension of the substrate	150 mm × 150 mm × 10 mm
The mesh size of the substrate	5 mm
The mesh size of the deposition layers	1 mm

Since the WAAM forming process is characterized by three-dimensional nonlinear transient thermal action, its heat transfer control satisfies the three-dimensional nonlinear transient thermal governing equation. The governing equation is expressed as follows [28]:

$$\rho c \frac{\partial T}{\partial t} = \frac{\partial}{dx}\left(k_x \frac{\partial T}{\partial x}\right) + \frac{\partial}{d_y}\left(k_y \frac{\partial T}{\partial y}\right) + \frac{\partial}{d_z}\left(k_z \frac{\partial T}{\partial z}\right) + \rho\Omega \quad (1)$$

In the equation, k_x, k_y, and k_z are the thermal conductivity of the material in three directions; ρ is the density of the material; c is the specific heat capacity; T is the temperature; Ω is the intensity of the internal heat source; t is the time for heat transfer.

The temperature field was calculated using the double-ellipsoidal heat source in order to accurately simulate the temperature distribution of arc heat during the WAAM. The heat distribution of the front and rear half ellipsoids could be calculated by Equation (2) and Equation (3), respectively.

$$Q_1 = \frac{6\sqrt{3} f_1 Q}{\pi a b_1 c \sqrt{\pi}} \exp\left[-3\left(\frac{x^2}{a^2} + \frac{y^2}{b_1^2} + \frac{z^2}{c^2}\right)\right] \quad (2)$$

$$Q_2 = \frac{6\sqrt{3} f_2 Q}{\pi a b_2 c \sqrt{\pi}} \exp\left[-3\left(\frac{x^2}{a^2} + \frac{y^2}{b_2^2} + \frac{z^2}{c^2}\right)\right] \quad (3)$$

In the formula, Q_1 and Q_2 are the arc heat input, a, b_1, b_2, and c represent the shape parameters of the ellipsoid, x, y, and z refer to the locations of the heat source, f1 and f2 are the heat distribution coefficients, and f1 + f2 = 2, usually f1 = 0.6 and f2 = 1.4 [27].

3. Results and discussion

3.1. Analysis of the thermal simulation

According to the numerical simulation, Figure 3(a) shows the results of the thermal field simulation when deposited to the 7th layer, and the temperature and heat flux curves for the 7th layer are displayed in Figure 3(b) and (c), respectively. The temperature distribution cloud map obtained from the infrared thermal imager during the WAAM processing is shown in Figure 3(d). At the moment when the deposition of the 7th layer is completed, the temperature at the point P0 of the 7th layer is 573.8 ℃, which was calculated as 582.55 ℃ through numerical calculation in Figure 3(a). As for thermal imaging, the diagonal field of view (DFOV) is 15.6°; the resolution is 300 ppi; the frame rate is 25 Hz.

With the results obtained from numerical simulation and aided by the equation, we can know the cooling rate, the temperature gradient, and the solidification rate of the material during the deposition process.

The cooling rate [29] is expressed as follows:

$$\frac{\partial T}{\partial t} = \left|\frac{T_L - T_s}{t_L - t_s}\right| \quad (4)$$

Where T_L and T_s refer to the liquid and solid phase temperatures of the super-invar alloy, respectively. According to the results calculated by JMatPro software, the T_L and T_s are 1726.02 K (1452.87 ℃) and 1653.15 K (1380 ℃). In addition, t_L and t_s are the times when the super-invar alloy reached the liquid and solid phase temperature, respectively.

The temperature gradient is expressed as follows:

$$G = |\nabla T| = \left|\frac{q}{k}\right| \quad (5)$$

In the expression, |q| refers to the value of the heat flow density, which can be acquired from the results of simulation [30]. Correspondingly, k is the thermal conductivity of the super-invar alloy at the liquid temperature, which was calculated as 33.46 $W \cdot m^{-1} \cdot k^{-1}$ through JMatPro software.

The solidification rate [29] is expressed as follows:

$$R = \frac{1}{G}\frac{\partial T}{\partial t} \quad (6)$$

Based on the thermal simulation results and equations, the cooling rate at point P0 of the 7th layer when the deposition of the 7th layer is completed was calculated as 105.77 K/s; the temperature gradient was 129707 K/m; the solidification rate was 0.000815 m/s.

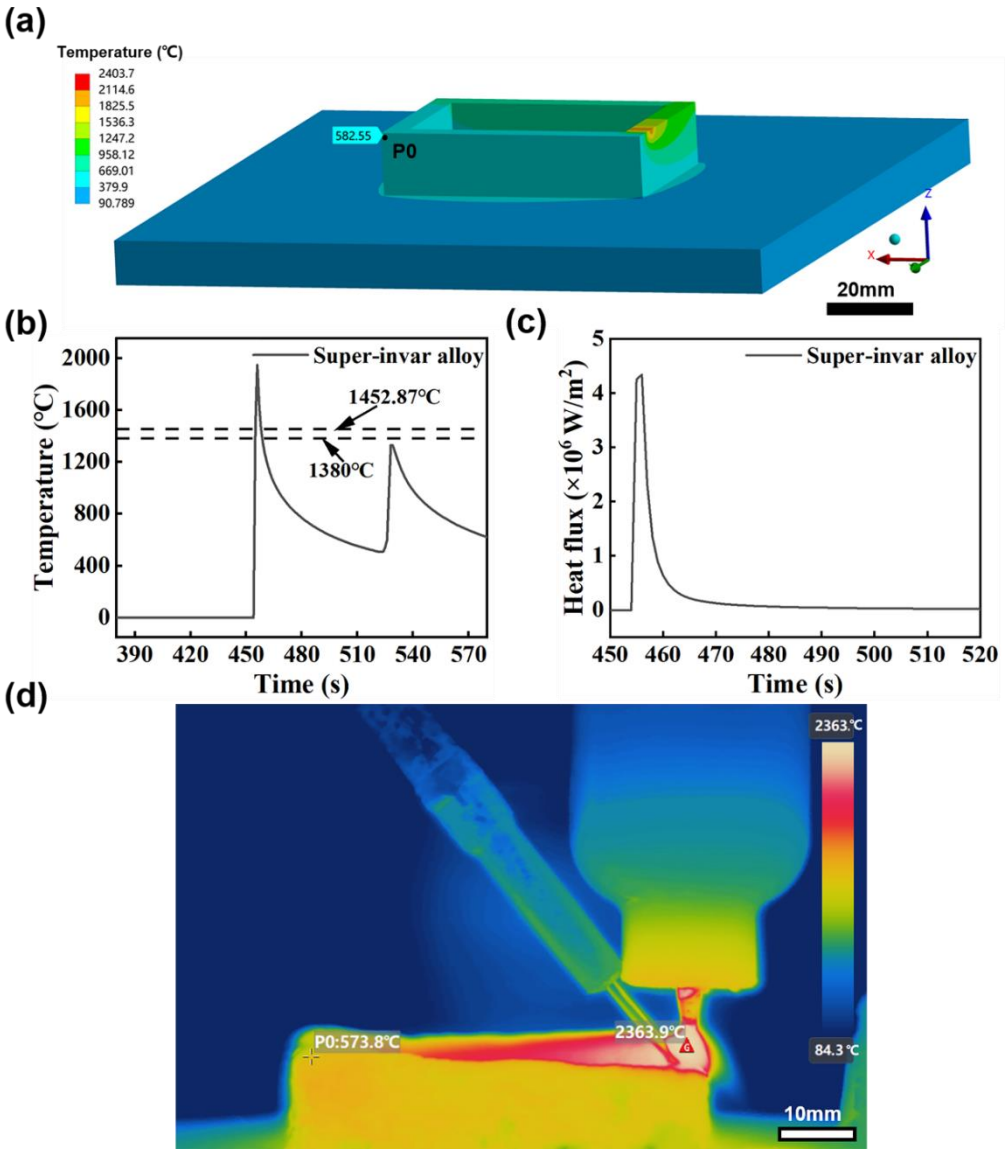

Figure 3. Simulation and experiment results: **(a)** Temperature distribution cloud map of the 7th layer in simulation; **(b)** The temperature curves at point P0 of the 7th layer in simulation; **(c)** The heat flux curves at point P0 of the 7th layer in simulation; **(d)** Temperature distribution cloud map of the 7th layer by infrared thermal imager during WAAM experiment.

3.2. Macrostructure and manufacturing process

The manufactured super-invar thin-wall rectangular component by WAAM was shown in Figure 4, including building direction view and scanning direction view. The dimensions were about 60 (length) × 40 (width) × 55 (height) mm, with a wall thickness of about 7 mm.

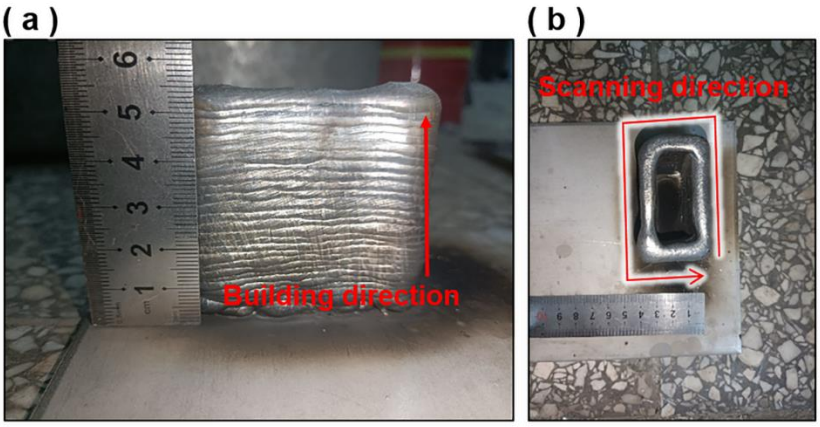

Figure 4. Thin-wall rectangular part by WAAM: **(a)** Front view; **(b)** Vertical view.

During the deposition process, the transfer mode of a liquid metal droplet has a significant impact on the stability of the deposition process and the geometric accuracy of the deposition [31]. The molten metal transfer process observed by a high-speed camera during one current cycle is shown in Figure 5. During the base current time, the arc continues to burn and the metal wire is melted to form the droplet; meanwhile, due to the long base current time, the droplet grows with time. When the peak current time comes, the metal droplet is transferred into the molten under the influence of gravity and the pulsed arc force [32]. After that, a new droplet forms and grows during the base current time.

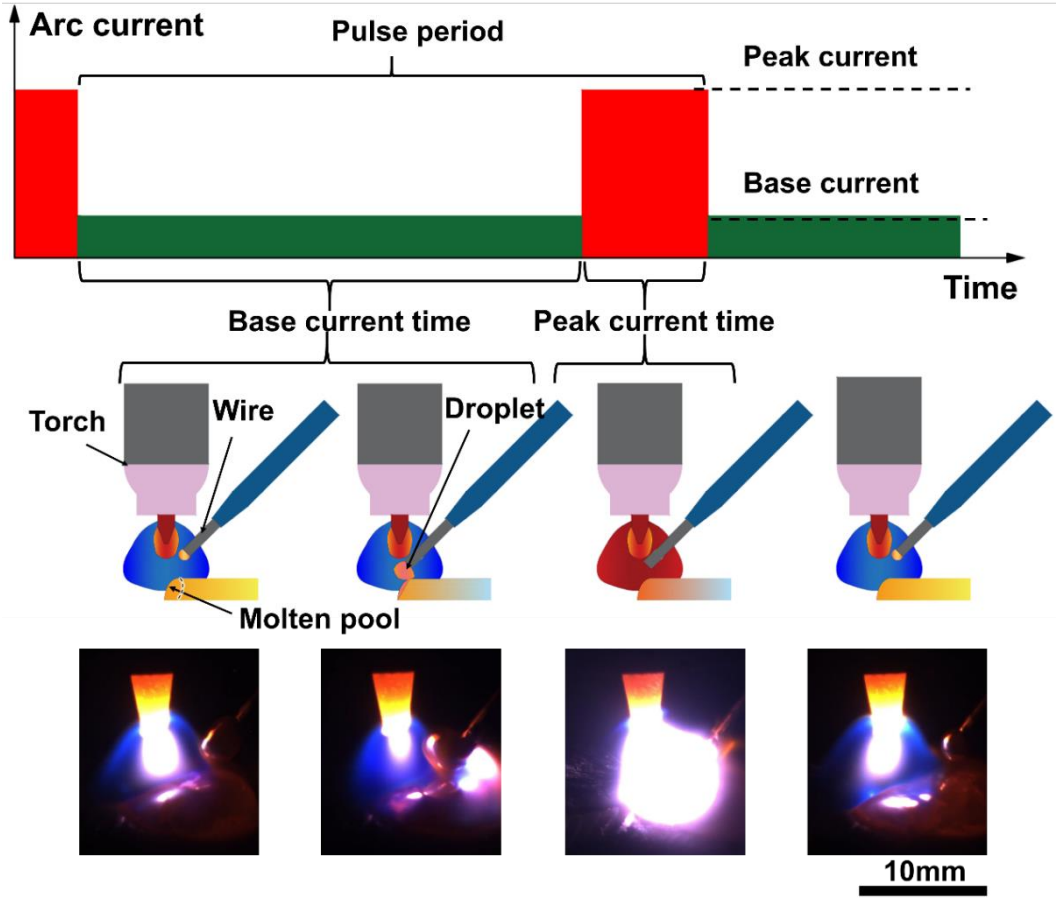

Figure 5. The complete process of molten metal transfer in a single current pulse cycle.

According to previous studies, there are three determined behaviors of metal transfer during AM processes: droplet transfer mode, intermediate transfer mode, and liquid bridge transfer mode [33]. The transfer modes are mainly governed by the wire feeding position [34]. As the wire feeding position increases, the metal transfer mode changes from liquid transfer to intermediate transfer, then to droplet transfer. Among three metal transfer modes, liquid bridge transfer is the most desirable metal transfer mode [35], which minimizes the impact on the molten pool and guarantees a better surface of the deposited parts. For liquid bridge mode during the deposition process, a steady liquid metal bridge is formed by the droplets' persistent contact with the molten pool, allowing fluid to continuously flow from the metal wire into the molten pool [36]. According to Figure 5, the metal transfer mode in this experiment is liquid bridge transfer. Ma *et al.* [37] also found the liquid bridge transfer mode in the study on laser welding stainless steel.

3.3. Microstructure

Figure 6 displays the image of the metallographic microstructure acquired using an optical microscope. The three-dimensional reconstruction diagram of the microscopic morphologies of the specimen is shown in Figure 6(a). By analyzing the microstructure morphology in different orientations, the microstructure of the specimen is three-dimensional columnar grains, which are growing through the molten pool in a direction perpendicular to the molten pool. The columnar grains in the middle position are larger than those on either side. Liu *et al.* [38] indicate that the main microstructural characteristic of additive manufacturing materials is columnar grains formed by crystals growing epitaxially from the molten pool boundary. Yang *et al.* [39] pointed out that remelting is the cause of epitaxial growth of grains, and only the grains near the molten pool's boundary was remelted.

The larger size of the columnar grains in the middle position is related to the temperature gradient and cooling rate. The concentration of heat from the arc is in the center region with a larger temperature gradient than on the sides, while the cooling rate is determined by the way the heat is dissipated from the molten pool. During the deposition process, there are three ways to dissipate heat from the molten pool: heat conduction via the substrate and previously deposited layers, heat conduction through the air, and thermal radiation [40]. In the center position, the molten pool can only dissipate heat through the layer of prior deposit; when it is on either side, it may release heat through the air as well as the layer of previous deposit, which causes cooling to occur more quickly. As a consequence, the large temperature gradient leads to faster growth in the middle position, while the slow cooling rate makes the growth time longer as well, resulting in larger columnar grain sizes in the middle region and smaller sizes in the regions on either side.

A few microstructure images in the thickness direction are shown in Figure 6(b–e), from which it can be seen that many sub-grains with a cellular structure are observed inside each columnar grain. Cui *et al.* [41] also observed a similar cellular structure in 316L stainless steel. As shown in Figure 6(b), there are many columnar grains growing across the melt pool boundary, which is due to the remelting of the lower grains during the deposition of the upper sample. As demonstrated in Figure 6(c), the development orientation of the cellular sub-grains is consistent within each columnar grain, although it differs amongst grains. In addition, the cellular sub-grains have different morphologies. In Figure 6(d), the cellular sub-grains show the morphology of prismatic cells, while in Figure 6(e), they show the morphology of elongated cells.

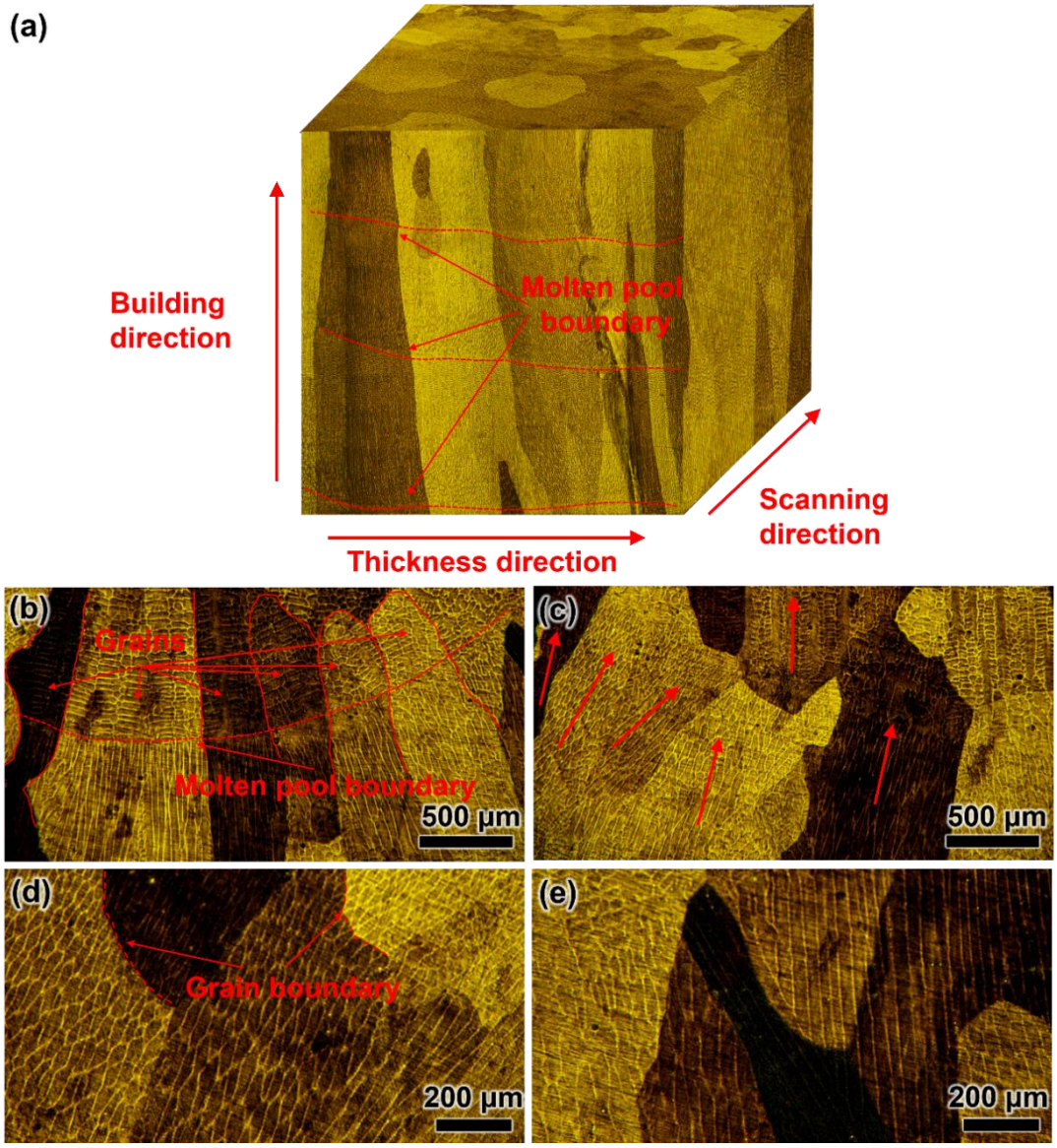

Figure 6. The microscopic morphologies of the specimen: **(a)** The three-dimensional reconstruction diagram; **(b–e)** The typical cellular microstructures.

It is recognized that in additive manufacturing, the morphology of the resulting microstructure is correlated with the temperature gradient G and solidification rate R during the deposition process [42]. From directional solidification theory, with the gradual decrease of G/R, the planar morphology changes into columnar cellular, followed by columnar dendrites, and finally to equiaxed crystal [43]. When G/R is above 5×10^{10} K·s·m^{-2}, it would be planar [44], and it could be equiaxed grain only when the value of $G^{3.4}/R$ is less than 10^4 [45]. According to the calculation results above, the G/R is 1.59×10^8 K·s·m^{-2}, and the value of $G^{3.4}/R$ is 3.12×10^5; consequently, the microstructure of the super-invar alloy is not planar or equiaxed crystal. In a study conducted by Chen *et al.* [46], the columnar cellular crystal was found in stainless steel, and the G/R of the stainless steel is 1.42×10^8 K·s·m^{-2}. Based on the above analysis, the microstructure of the super-invar alloy should be a columnar cellular structure, as shown in Figure 7.

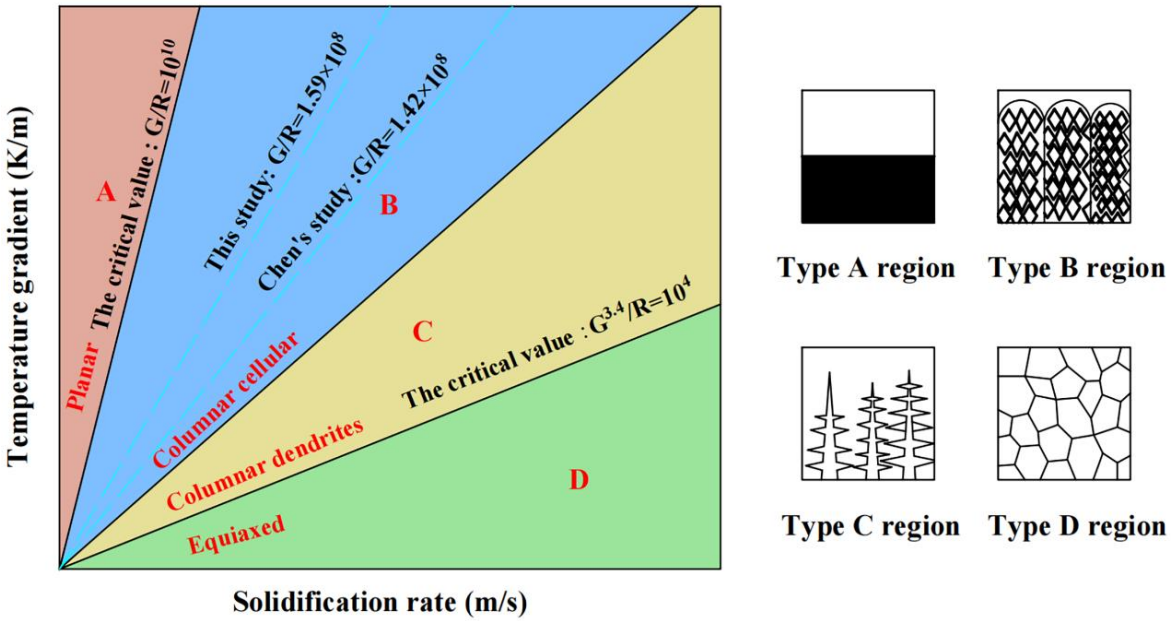

Figure 7. The relationship between different morphologies of microstructure and G/R [44–46].

The formation of cellular sub-grains is associated with a high cooling rate. During the additive manufacturing process, since the cooling rate is very high, there is insufficient time to develop the secondary dendrite arm, and thus only cellular structure is observed [47]. According to the studies of Voisin *et al.* [48], the three-dimensional structure of the cellular sub-grains is a tetragonal prism-like structure. As shown in Figure 8, because of the cellular sub-grains' various orientations, different prismatic and elongated cellular morphologies can be observed under a microscope.

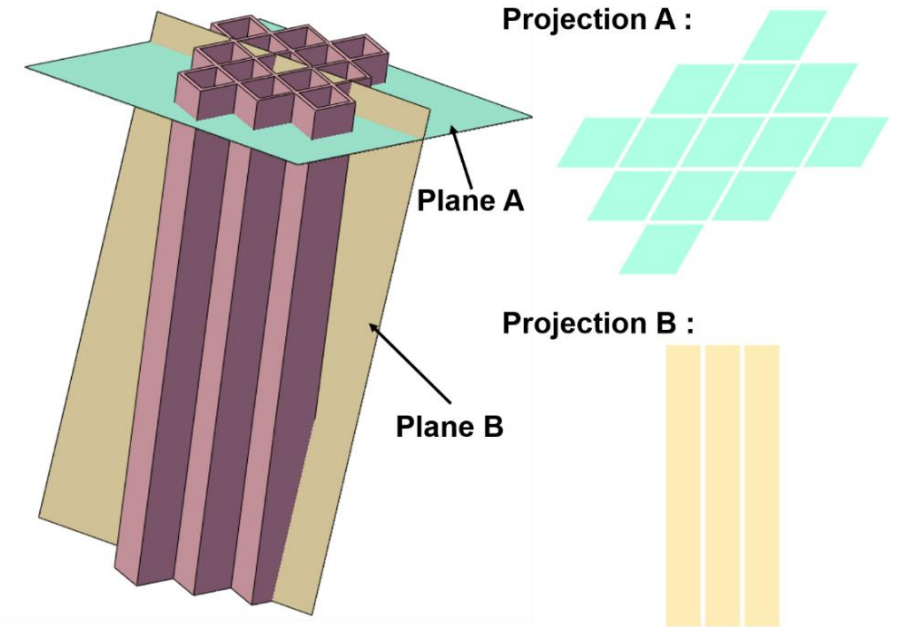

Figure 8. Three-dimensional structure of the cellular sub-grains.

The diffraction pattern quality map of EBSD is displayed in Figure 9(a). The red line represents high-angle grain boundaries, while the blue line represents low-angle grain boundaries. It is evident that the specimen has a significant number of high-angle grain boundaries, and statistical analysis indicates

that these boundaries account for 72.4% of the total. The findings imply that there is considerable diversity in the orientation of the individual grains. Figure 9(b) shows the color-coded representation of the crystallographic orientation, which also indicates the random orientation of the grains. The inverse pole figures (IPF) at three directions of specimens show that there is no obvious texture because of the low strength of the crystal orientation aggregation, as shown in Figure 9(c).

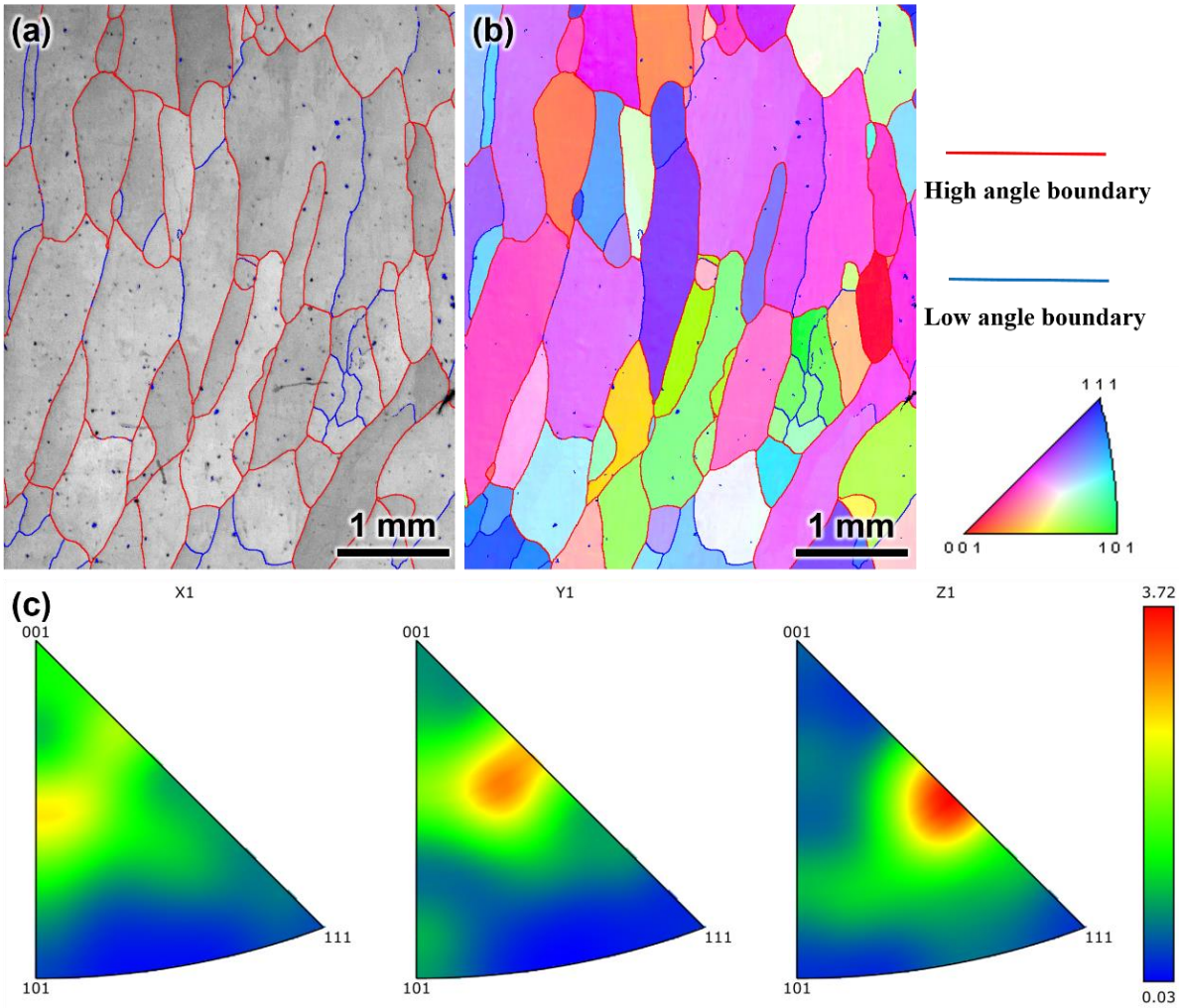

Figure 9. Graph of EBSD analysis results: **(a)** The diffraction pattern quality map; **(b)** The grain orientation map; **(c)** The inverse pole figures.

3.4. Hardness and tensile behavior

The Vickers hardness test was used to indirectly determine the overall microstructure uniformity on the surface of specimens. As shown in Figure 10 (the side of point O near the bottom of the super-invar alloy specimen), the measurement results of 90 points were taken on a 6 mm × 60 mm area along the building direction. Along the deposition direction, the average hardness value is 152$HV_{0.2}$. It is evident that the hardness of the specimen is uniformly distributed along the deposition direction because the difference in hardness of the measured samples does not exceed 10$HV_{0.2}$. This result can be attributed to the reasonable regulation of the process parameters, which results in a similar thermal cycle in each grain layer, a similar morphology of solidification, and a lack of numerous porosity defects, all of which contribute to a uniform distribution of microscopic hardness.

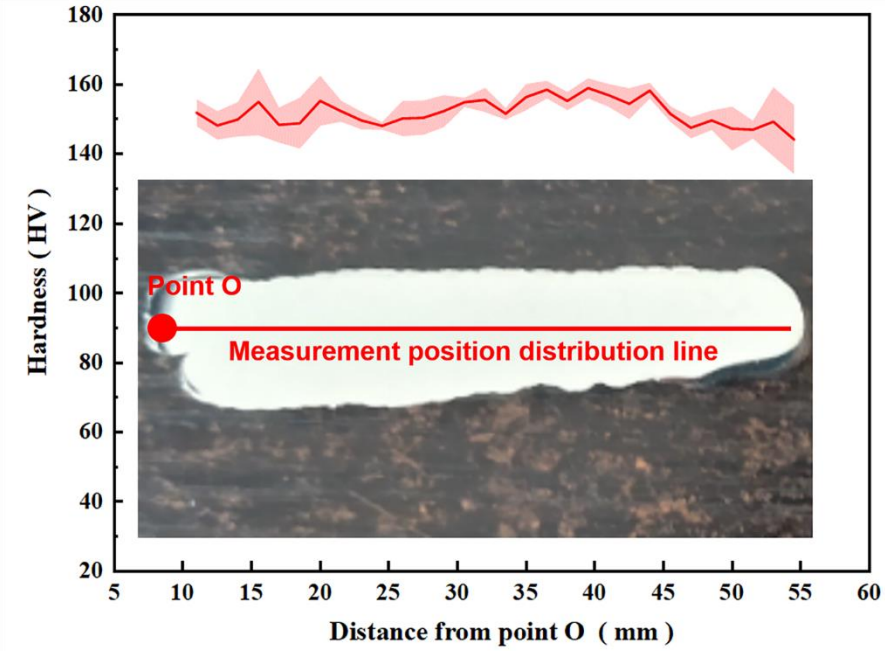

Figure 10. Hardness distribution curve (The light red area reflects the standard deviation of the measurement data).

In order to assess the mechanical properties of the heat-treated samples, tensile tests were conducted at room temperature. The results of these tests for the super-invar alloy samples are displayed in Figure 11(a), while typical transverse (HT) and longitudinal (VT) stress-strain curves are displayed in Figure 11(b). According to Table 4, the average strength and elongation of the longitudinal samples (average UTS: 398.8 MPa, average YS: 291.4 MPa, average elongation: 40.8%) are higher than that of the transverse samples (average UTS: 372.8 MPa, average YS: 263.3 MPa, average elongation: 33.8%). According to the typical stress-strain curves of two directions, super-invar alloy exhibits significant anisotropy.

The microstructure of additive manufactured samples affects their mechanical properties; cellular sub-grains have a major impact on tensile properties, improving the material's tensile strength as well as its ductility [49]. Because of the small size of the cellular sub-grains, expanding the sub-grain boundaries can hinder the movement of dislocations so that the mechanical strength of the material increases. However, it cannot completely prevent dislocations from passing through the sub-grain boundaries like traditional grain boundaries can [50]. We only discuss the contribution of cellular sub-grains, the values of grain refinement strengthening (σ_g) can be obtained by Hall-Petch equation [51]:

$$\sigma_g = k_y d^{-\frac{1}{2}} \tag{7}$$

In equation, k_y stands for the strengthening coefficient (24.70 MPa·mm$^{0.5}$ for austenite steel [52]); d is the size of the cellular sub-grains. According to Figure 6(d), d is 50.96 μm measured by ImageJ software. Therefore, the values of σ_g is 109.4 MPa. Other strengths may be contributed by the solid solution strengthening, the dislocation strengthening and the precipitation strengthening [53].

Table 4. The mechanical properties of specimens tested along HT and VT directions.

Direction	YS (MPa)	UTS (MPa)	Elongation (%)
HT	263.3 ± 5.8	372.8 ± 2.6	33.8 ± 3.8
VT	291.4 ± 6.2	398.8 ± 7.6	40.8 ± 4.1

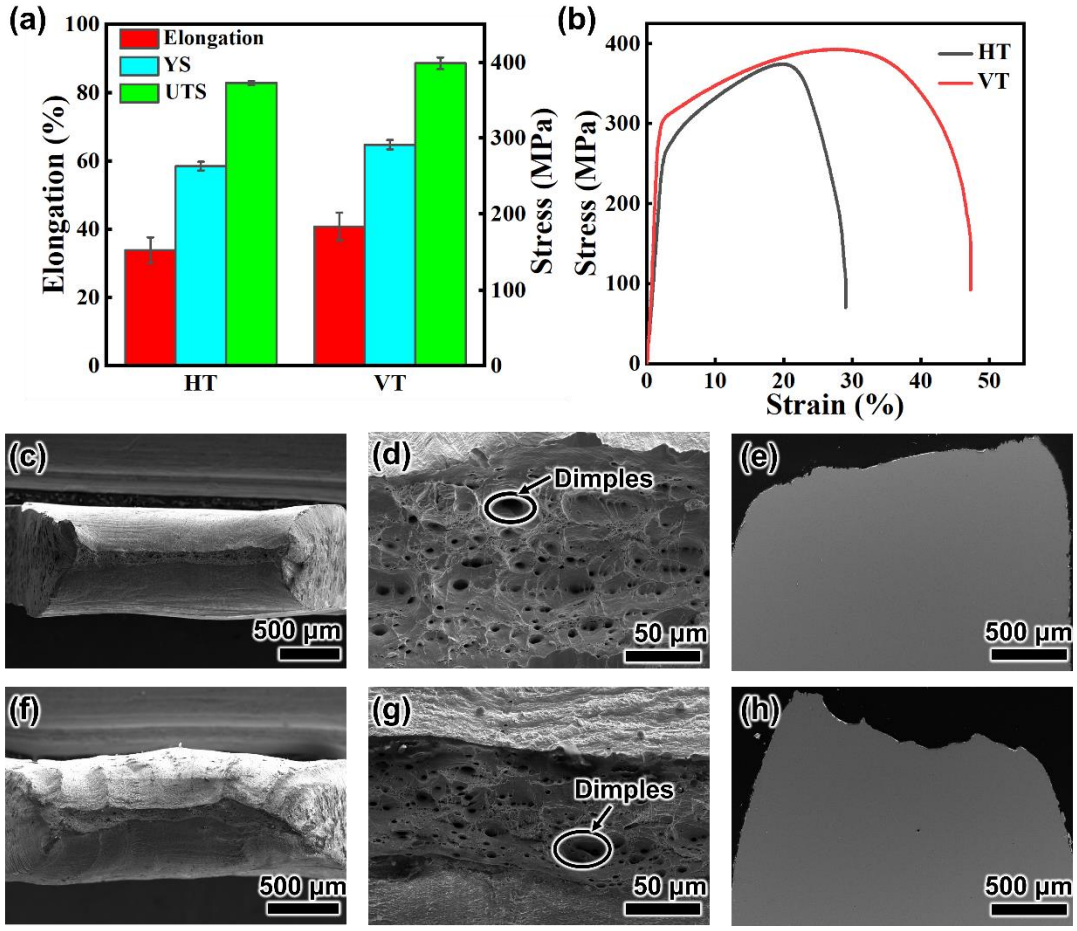

Figure 11. (a) Average strength of the tensile test; **(b)** Stress-strain curves of super-invar alloy; **(c–d)** SEM image of the transverse fracture surfaces; **(e)** SEM image of the transverse side-view fracture; **(f–g)** SEM image of the longitudinal fracture surfaces; **(h)** SEM image of the longitudinal side-view fracture.

Figure 11(c–h) reveals the tensile fracture surfaces of super-invar alloy at room temperature. In Figure 11(c–h), a large number of dimples are distributed on the fracture surfaces, indicating ductile fracture in all examined tensile specimens. Jiao *et al.* [54] also found similar results in research of invar alloy using WAAM. Figure 11(c) and (f) show that the transverse fracture has a flatter fracture surface than the longitudinal fracture, which has a more irregular fracture surface. This is because the longitudinal fracture experiences more intense deformation during the fracture process, indicating better longitudinal plasticity in the material, which is consistent with the structure found in tensile tests. As shown in Figure 11(d) and (g), there are more dimples in the longitudinal fracture, which can also indicate that the longitudinal specimens are tougher and have higher elongation. During specimen fracture, the transverse and longitudinal tensile specimen fracture sections are shown in Figure 11(e) and (h), and it is found that the specimen fracture does not have obvious cracks.

3.5. Thermal expansion behavior

The thermal expansion characteristics of the super-invar alloy have been investigated in a temperature range of 20 ℃ to 100 ℃, as presented in Figure 12. In the temperature range between 20 ℃ and 100 ℃,

the specimen has a very low CTE; the slope of each point on the curve is the CTE at the temperature; the average CTE for the whole temperature range is 0.265×10^{-6} K^{-1}. The super-invar alloy has an extremely low CTE due to their spontaneous volume magnetostriction below the Curie temperature. According to research conducted by Lohaus *et al.* [55], as temperature increases, a negative thermal expansion coefficient produced by magnetism offsets the lattice's positive thermal expansion, which results in the invar effect. In addition, there is a strong correlation between the super-invar alloys' CTE and the content of Ni [56], which can affect the strength of spontaneous volume magnetostriction of the super-invar alloy.

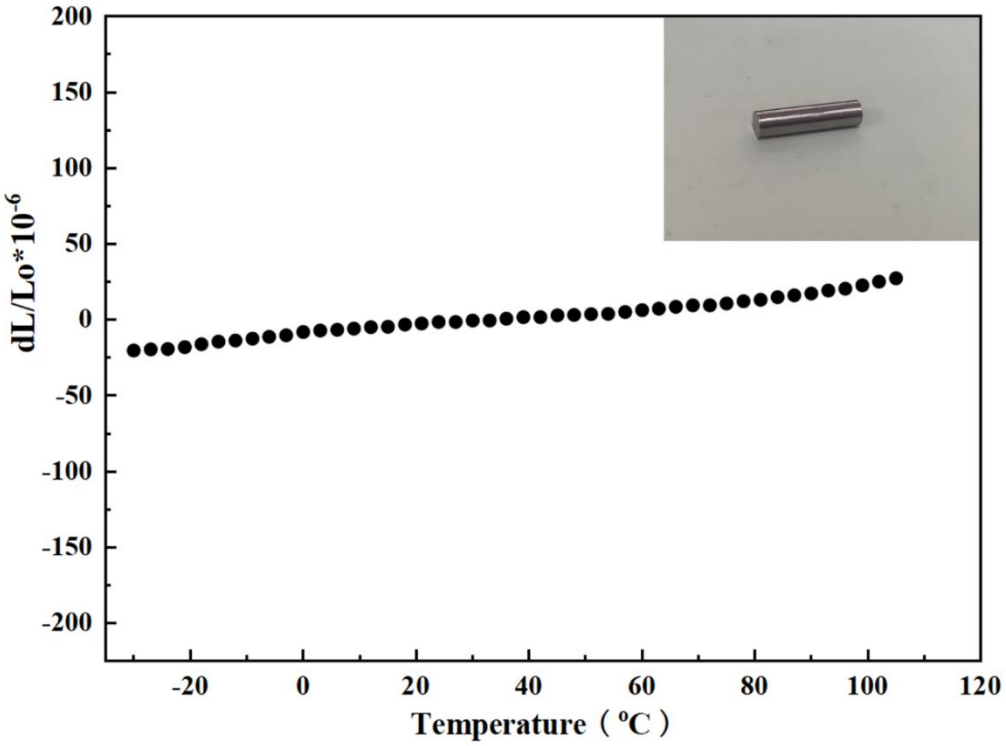

Figure 12. The curve of the CTE test results.

4. Conclusion

In this work, we have mainly investigated the microstructure and the mechanical property of a super-invar alloy (Fe64-Ni32-Co4, wt %) via WAAM, which provides an efficient pathway for the manufacturing of super-invar alloy components. The primary findings are summarized as follows:

(1) Based on the WAAM technology, a super-invar thin-wall rectangular component was obtained. The metal transfer mode during the deposition process was liquid bridge transfer. According to the finite element analysis results, the cooling rate was 105.77 K/s, the temperature gradient was 129707 K/m, the solidification rate was 0.000815 m/s, and the G/R was calculated as 1.59×10^{8} $K \cdot s \cdot m^{-2}$.

(2) The microstructure of super-invar alloy has columnar cellular morphologies. There are many cellular sub-grains with various orientations and morphologies inside the epitaxially grow columnar crystals, which grow in a direction perpendicular to the molten pool boundary line. The formation of the columnar cellular morphologies is associated with the G/R. There is no obvious texture in the super-invar alloy specimen. The hardness of the sample is uniformly distributed

along the deposition direction, with a 152$HV_{0.2}$ average hardness. The difference in hardness of all measured points does not exceed 10$HV_{0.2}$.

(3) The mechanical properties of super-invar alloy exhibit anisotropy. The longitudinal specimens have better mechanical properties; the average UTS is 398.8 MPa, the average YS is 291.4 MPa, and the average elongation is 40.8%. The average UTS of the transverse is 372.8 MPa, the average YS is 263.3 MPa, and the average elongation is 33.8%. Both longitudinal and transverse specimens have ductile fractures. Super-invar alloy samples have an extremely low coefficient of thermal expansion, which was measured to be 0.265 × 10^{-6} K^{-1} from 20 ℃ to 100 ℃.

Acknowledgments

This work was supported financially by the National Natural Science Foundation of China (52475320).

Conflicts of interest

The authors declare no conflict of interest.

Author's contribution

Shuijun Ye: Methodology, Formal analysis, Investigation, Writing-original draft. Lindong Xu: Methodology, Investigation, Writing-review & editing. Yueling Guo: Conceptualization, Methodology, Investigation, Writing-review & editing, Funding acquisition. Xinglong Di: Specimen manufacturing, Methodology, Investigation, Writing-review & editing. Qifei Han: Methodology, Investigation, Writing-review & editing. Yuanxuan Zheng: Methodology, Data curation. Xingchen Li: Investigation, Writing-review & editing.

References

[1] Singh RS, Guruswamy S. Elastic constants of equiatomic Fe–Ni Invar alloy single crystal. *Aip Adv* 2023, 13(11):115112.

[2] Chen C, Xie Y, Liu L, Zhao R, Jin X, *et al.* Cold spray additive manufacturing of Invar 36 alloy: microstructure, thermal expansion and mechanical properties. *J. Mater. Sci. Technol.* 2021, 72:39–51.

[3] Asgari H, Salarian M, Ma H, Olubamiji A,Vlasea M. On thermal expansion behavior of invar alloy fabricated by modulated laser powder bed fusion. *Mater. Des.* 2018, 160:895–905.

[4] Yakout M, Elbestawi MA, Veldhuis SC. A study of thermal expansion coefficients and microstructure during selective laser melting of Invar 36 and stainless steel 316L. *Addit. Manuf.* 2018, 24:405–418.

[5] Wang H, Hu S, Shen J, Li D,Lu J. Effect of duty cycle on microstructure and mechanical properties of pulsed GTAW lap joint of Invar. *J. Mater. Process. Technol.* 2017, 243:481–488.

[6] Wegener T, Brenne F, Fischer A, Möller T, Hauck C, *et al.* On the structural integrity of Fe-36Ni Invar alloy processed by selective laser melting. *Addit. Manuf.* 2021, 37:101603.

[7] Jafari D, Vaneker THJ, Gibson I. Wire and arc additive manufacturing: Opportunities and challenges to control the quality and accuracy of manufactured parts. *Mater. Des.* 2021, 202:109471.

[8] Fu R, Tang S, Lu J, Cui Y, Li Z, *et al.* Hot-wire arc additive manufacturing of aluminum alloy with

reduced porosity and high deposition rate. *Mater. Des.* 2021, 199:109370.
[9] Huang G, He G, Liu Y, Huang K. Anisotropy of microstructure, mechanical properties and thermal expansion in Invar 36 alloy fabricated via laser powder bed fusion. *Addit. Manuf.* 2024, 82:104025.
[10] Wei K, Yang Q, Ling B, Yang X, Xie H, *et al.* Mechanical properties of Invar 36 alloy additively manufactured by selective laser melting. *Mater. Sci. Eng. A* 2020, 772:138799.
[11] Sood A, Schimmel J, Ferreira VM, Bosman M, Goulas C, *et al.* Directed energy deposition of Invar 36 alloy using cold wire pulsed gas tungsten arc welding: Effect of heat input on the microstructure and functional behaviour. *J. Mater. Res. Technol.* 2023, 25:6183–6197.
[12] Aldalur E, Suárez A, Veiga F. Thermal expansion behaviour of Invar 36 alloy parts fabricated by wire-arc additive manufacturing. *J. Mater. Res. Technol.* 2022, 19:3634–3645.
[13] Ostolaza M, Arrizubieta JI, Lamikiz A, Plaza S,Ortega N. Latest Developments to Manufacture Metal Matrix Composites and Functionally Graded Materials through AM: A State-of-the-Art Review. *Materials* 2023, 16(4):1746.
[14] Su JL, Jiang FL, Teng J, Chen LQ, Requena G, *et al.* Laser additive manufacturing of titanium alloys: process, materials and post-processing. *Rare Met.* 2024, 43(12):6288–6328.
[15] Su J, Jiang F, Teng J, Chen L, Yan M, *et al.* Recent innovations in laser additive manufacturing of titanium alloys. *Int. J. Extreme Manuf.* 2024, 6(3):032001.
[16] Chen J, Chen B. Progress in Additive Manufacturing of Magnesium Alloys: A Review. *Materials* 2024, 17(15):3851.
[17] Xia C, Pan Z, Polden J, Li H, Xu Y, *et al.* A review on wire arc additive manufacturing: Monitoring, control and a framework of automated system. *J. Manuf. Syst.* 2020, 57:31–45.
[18] Su J, Ng WL, An J, Yeong WY, Chua CK, *et al.* Achieving sustainability by additive manufacturing: a state-of-the-art review and perspectives. *Virtual Phys. Prototyping* 2024, 19(1):e2438899.
[19] Jiao G, Fang X, Chen X, Xi N, Zhang M, *et al.* The origin of low thermal expansion coefficient and enhanced tensile properties of Invar alloy fabricated by directed energy deposition. *J. Mater. Process. Technol.* 2023, 317:117994.
[20] Veiga F, Suárez A, Artaza T,Aldalur E. Effect of the Heat Input on Wire-Arc Additive Manufacturing of Invar 36 Alloy: Microstructure and Mechanical Properties. *Weld. World* 2022, 66(6):1081–1091.
[21] Ke WC, Oliveira JP, Cong BQ, Ao SS, Qi ZW, *et al.* Multi-layer deposition mechanism in ultra high-frequency pulsed wire arc additive manufacturing (WAAM) of NiTi shape memory alloys. *Addit. Manuf.* 2022, 50:102513.
[22] Yan Y, Si J, Di X, Guo Y, Han Q, *et al.* Minimizing porosity and optimizing microstructure of hot-wire arc additive manufactured Al-Cu-Mg-Ag alloy for strength increment. *J. Manuf. Processes* 2024, 118:89–102.
[23] Lu T, Liu C, Li Z, Wu Q, Wang J, *et al.* Hot-wire arc additive manufacturing Ti–6.5Al–2Zr–1Mo–1V titanium alloy: Pore characterization, microstructural evolution, and mechanical properties. *J. Alloys Compd.* 2020, 817:153334.
[24] Xu T, Zhang M, Wang J, Lu T, Ma S, *et al.* Research on high efficiency deposition method of titanium alloy based on double-hot-wire arc additive manufacturing and heat treatment. *J. Manuf. Processes* 2022, 79:60–69.
[25] Xu T, Liu J, Wang J, Lu T, Ma S, *et al.* Layer control method and mechanical anisotropy of titanium

alloy based on double-hot-wire arc additive manufacturing. *J. Manuf. Processes* 2022, 82:448–460.
[26] Li Z, Liu C, Xu T, Ji L, Wang D, *et al.* Reducing arc heat input and obtaining equiaxed grains by hot-wire method during arc additive manufacturing titanium alloy. *Mater. Sci. Eng. A* 2019, 742:287–294.
[27] Goldak J, Chakravarti A, Bibby M. A new finite element model for welding heat sources. *Metall. Trans. B* 1984, 15(2):299–305.
[28] Liu H, Du X, Guo H, Liu J, Chen P, *et al.* Finite element analysis of effects of dynamic preheating on thermal behavior of multi-track and multi-layer laser cladding. *Optik* 2021, 228:166194.
[29] Han Q, Guo Y, Hu J, Fu R, Yan Y, *et al.* Superior strength-ductility synergy of wire-arc directed energy deposited Mg-Al-Si alloys mediated by sub-rapid solidification. *J. Magnesium Alloys* 2024, 12(11):4594–4609.
[30] Fu R, Yu Z, Wu Q, Liu C. Microstructure evolution and property strengthening of Ti2AlNb alloys prepared by multi-wire arc-directed energy deposition. *J. Mater. Process. Technol.* 2024, 329:118460.
[31] Huang J, Yuan W, Yu S, Zhang L, Yu X, *et al.* Droplet transfer behavior in bypass-coupled wire arc additive manufacturing. *J. Manuf. Processes* 2020, 49:397–412.
[32] Luo Y, Li J, Xu J, Zhu L, Han J, *et al.* Influence of pulsed arc on the metal droplet deposited by projected transfer mode in wire-arc additive manufacturing. *J. Mater. Process. Technol.* 2018, 259:353–360.
[33] Wang C, Suder W, Ding J, Williams S. The effect of wire size on high deposition rate wire and plasma arc additive manufacture of Ti-6Al-4V. *J. Mater. Process. Technol.* 2021, 288:116842.
[34] Ríos S, Colegrove PA, Williams SW. Metal transfer modes in plasma Wire + Arc additive manufacture. *J. Mater. Process. Technol.* 2019, 264:45–54.
[35] Hu R, Luo M, Liu T, Liang L, Huang A, *et al.* Thermal fluid dynamics of liquid bridge transfer in laser wire deposition 3D printing. *Sci. Technol. Weld. Joining* 2019, 24(5):401–411.
[36] Ke W, Yan W, Oliveira JP, Pang B, Chen L, *et al.* Thermal-fluid behavior, microstructure and mechanical properties in liquid bridge transfer mode during directed energy deposition-arc additive manufacturing—Insights using NiTi as a model alloy. *Addit. Manuf.* 2023, 77:103807.
[37] Ma G, Li L, Chen Y. Effects of beam configurations on wire melting and transfer behaviors in dual beam laser welding with filler wire. *Opt. Laser Technol.* 2017, 91:138–148.
[38] Liu Z, Zhao D, Wang P, Yan M, Yang C, *et al.* Additive manufacturing of metals: Microstructure evolution and multistage control. *J. Mater. Sci. Technol.* 2022, 100:224–236.
[39] Yang M, Wang L, Yan W. Phase-field modeling of grain evolutions in additive manufacturing from nucleation, growth, to coarsening. *npj Comput. Mater.* 2021, 7(1):56.
[40] Li H, Chen B, Tan C, Song X, Feng J. Microstructure evolution and mechanical properties of laser metal deposition of Invar 36 alloy. *Opt. Laser Technol.* 2020, 125:106037.
[41] Cui L, Jiang F, Deng D, Xin T, Sun X, *et al.* Cyclic response of additive manufactured 316L stainless steel: The role of cell structures. *Scr. Mater.* 2021, 205:114190.
[42] Yu Y, Wang L, Zhou J, Li H, Li Y, *et al.* Impact of fluid flow on the dendrite growth and the formation of new grains in additive manufacturing. *Addit. Manuf.* 2022, 55:102832.
[43] Dai T, Gu D, Qiu Y, Guo W, Ding H, *et al.* An experimental study on effects of temperature gradient on microstructure of a 308L stainless steel manufactured by directed energy deposition. *J. Iron.*

Steel Res. Int. 2024, 31(8):2031–2040.
[44] Scipioni Bertoli U, MacDonald BE, Schoenung JM. Stability of cellular microstructure in laser powder bed fusion of 316L stainless steel. *Mater. Sci. Eng. A* 2019, 739:109–117.
[45] Lekakh SN, O'malley R, Emmendorfer M,Hrebec B. Control of Columnar to Equiaxed Transition in Solidification Macrostructure of Austenitic Stainless Steel Castings. *ISIJ International* 2017, 57(5):824–832.
[46] Chen A, Jiang J, Li X, Hou J, Ding Z, *et al.* Formation and effect of hierarchical structures on corrosion performance of stainless steel bipolar plate fabricated by powder bed fusion. *Corros. Sci.* 2023, 219:111193.
[47] Wang D, Song C, Yang Y, Bai Y. Investigation of crystal growth mechanism during selective laser melting and mechanical property characterization of 316L stainless steel parts. *Mater. Des.* 2016, 100:291–299.
[48] Voisin T, Forien JB, Perron A, Aubry S, Bertin N, *et al.* New insights on cellular structures strengthening mechanisms and thermal stability of an austenitic stainless steel fabricated by laser powder-bed-fusion. *Acta Mater.* 2021, 203:116476.
[49] Barkia B, Aubry P, Haghi-Ashtiani P, Auger T, Gosmain L, *et al.* On the origin of the high tensile strength and ductility of additively manufactured 316L stainless steel: Multiscale investigation. *J. Mater. Sci. Technol.* 2020, 41:209–218.
[50] Kong D, Dong C, Wei S, Ni X, Zhang L, *et al.* About metastable cellular structure in additively manufactured austenitic stainless steels. *Addit. Manuf.* 2021, 38:101804.
[51] Liu H, Yu Y, Feng L, Wang Y, Sun Z, *et al.* Promoting nanoprecipitates via prefabricated defects to pin dislocations and grain boundaries for trading off high-strength and low-thermal-expansion of invar alloys. *J. Alloys Compd.* 2024, 994:174770.
[52] Wang Q, Dong Y, Jiang Z,Huang J. Enhancing low thermal expansion behavior and strength via induced Zr-rich intermetallic phase in Fe-36Ni Invar alloy. *Mater. Des.* 2023, 226:111644.
[53] Sui QS, Li JX, Zhai YZ, Sun ZH, Wu YF, *et al.* Effect of alloying with V and Ti on microstructures and properties in Fe–Ni–Mo–C invar alloys. *Materialia* 2019, 8:100474.
[54] Jiao G, Fang X, Zhang M, Li Z, Cai R, *et al.* Synergistic improvement of mechanical property and thermal expansion of Wire-arc DED Invar alloy enabled by a novel deposition strategy. *J. Manuf. Processes* 2024, 121:121–135.
[55] Lohaus SH, Heine M, Guzman P, Bernal-Choban CM, Saunders CN, *et al.* A thermodynamic explanation of the Invar effect. *Nat. Phys.* 2023, 19(11):1642–1648.
[56] Khmelevskyi S, Steiner S. Predictive Theory of Anomalous Volume Magnetostriction in Fe–Ni Alloys: Bond Repopulation Mechanism of the Invar Effect. *J. Phys. Chem. C* 2023, 128(1):605–612.